Numerical investigation of the surface and microstructure effects on the high cycle fatigue performance of additive manufactured stainless steel 316L

Xiaoyu Liang [a,b,c,*], Camille Robert [a], Anis Hor [b], Franck Morel [a]

[a] Angers Laboratory of Mechanics, Manufacturing Process and Innovation (LAMPA), Arts et Métiers Campus Angers, 49035 Angers Cedex, France
[b] Institut Clément Ader (ICA), Université de Toulouse, CNRS, ISAE-SUPAERO, UPS, INSA, Mines-Albi, 3 rue Caroline Aigle, 31400 Toulouse, France
[c] Department of Mechanical Engineering, Tsinghua University, Beijing 100084, China

Keywords:
Microstructure sensitive modeling
High cycle fatigue
Finite element method
Additive manufacturing
Stainless steel 316L

A B S T R A C T

This paper aims to study the individual and competitive effects of surface defects and microstructural components in an AM 316L by numerical methods. Based on the microstructure sensitive modeling framework, numerical simulations of models in different surface states with virtual quasi-realistic explicit microstructures are performed. Problems encountered during the establishment of the numerical polycrystalline aggregate model are discussed, including the grain morphology, the strongly textured microstructure with preferential crystallographic directions, roughness and surface defect. A statistical method based on generalized extreme value distribution along with a non-local method is used to describe the stochasticity of microstructural attributes. Simulations of differently configured explicit microstructure models are analyzed and discussed.

1. Introduction

As a complicated and much-studied phenomenon, fatigue relates to a broad range of aspects. But a comprehensive understanding is not yet achieved as the fast evolution of technologies brings out more new materials and new products. In this decade, Additive Manufacturing (AM) techniques undergo rapid advancements. Despite sharing the same chemical composition, the AM materials have distinct mechanical properties compared to that of the conventional ones [1,2]. More efforts are needed to complement the understandings, especially about the influences of inherent imperfect surface state and microstructure which is strongly dependent on the fabrication process on the fatigue behavior.

Among the AM techniques applied to metallic materials, selective laser melting (SLM) has received great attention because it accepts a large range of materials and produces high-functional components [3]. The surface quality is not only an aesthetic issue, but also a key factor for the success of SLM. The SLM parts in the as-built condition exhibit high surface imperfectness. The stair stepping effect, partially melted particles stuck on the surface, and unstable melt pool aggravate the surface roughness of SLM steels [4]. Independently from the alloy, surface roughness can be reduced by increasing the heat input while high thermal stresses lead to defect appearance in the meantime. Adding to that, the powder grades influence the surface roughness. Large particles induce higher surface roughness as compared to thinner counterparts [5]. Conventional surface treatment procedures (such as turning) create residual stresses and remove superficial defects from the material. They also compress near-surface defects by plastic deformation and reduce their negative effects on mechanical properties. The major drawback of these methods is that they cannot be used for parts with complex geometries. In terms of SLM 316L, several studies have proven that machining can decrease surface roughness leading to a higher fatigue life [6–8]. But the identified fatigue strengths are not always consistent. This is mainly attributed to differences in crack initiation mechanism, defect types, locations, material type and ductility [9]. In the as-built condition, cracks are generally induced by surface discontinuities, whereas machined or polished specimens exhibit crack initiation from surface roughness and internal defects.

The surface roughness and the defects are always considered to be detrimental to fatigue performance. But the exact role played by the microstructural attributes has not yet been thoroughly investigated and remains an open question. Specifically, products from SLM may exhibit a specific microstructure and contain multiple defects such as pores or lack-of-fusion. Their irregular shapes and pronounced sharpness result in a detrimental effect on the fatigue performance of the part [10]. Heat

* Corresponding author.
E-mail address: Xiaoyu.LIANG@ensam.eu (X. Liang).

https://doi.org/10.1016/j.ijfatigue.2021.106273

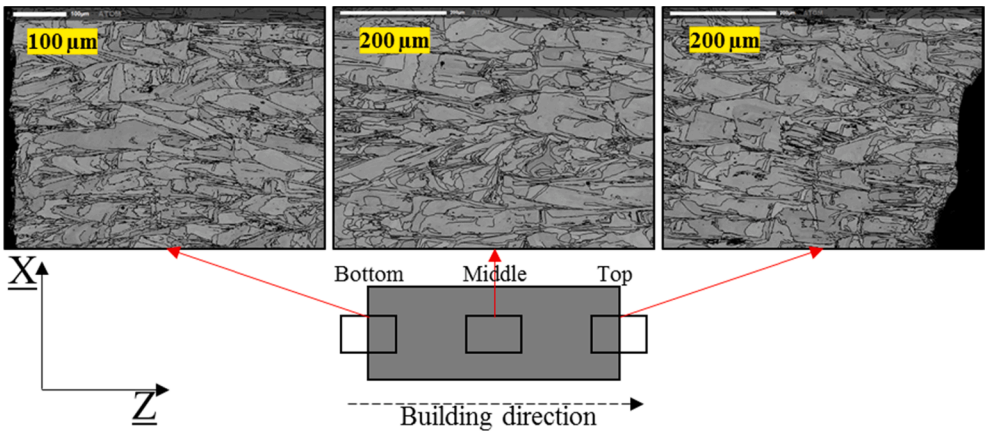

Fig. 1. BC maps of an SLM SS 316L: bottom, top and middle part of the sample.

treatment is often considered a common method to improve materials' performance. But the effects of different heat treatments on fatigue performance of SLM 316L lead to some controversy. Annealing does not necessarily change the high cycle fatigue performance or the polycrystalline microstructure [11]. The microstructure can be changed by Hot Isostatic Pressing (HIP) but the fatigue strength in the High Cycle Fatigue (HCF) regime seems sometimes to be unaffected [12]. Building direction which changes the texture of produced specimens is also found to influence fatigue behavior [13,14]. Moreover, the laser density used during fabrication may result in different fatigue performances [15]. The scatter of the fatigue strengths in the literature is no doubt originated from the distinct microstructures due to different configurations of fabrication and post-processing. Even though a large number of experimental investigations on fatigue behavior have been reported, it turns out that a numerical study is essential to answer some of the questions regarding the coupling effects of surface roughness, defects and microstructure on the fatigue strength of SLM 316L.

The numerical simulation of metallic polycrystalline aggregates for the fatigue predictions is more and more valued for efficiency and cost-saving as the fatigue experiments are very time consuming and require massive efforts on the devices' setting up and specimens' preparation. In order to take the effect of surface defects and microstructure into considerations, an explicit microstructure polycrystalline aggregate model is desired. Many differences can be enumerated between the microstructure of conventional material and that of AM material due to the special fabrication process. For instance, the AM products, especially those not heat-treated, often have a strongly textured microstructure and the grain size is usually non-constant. Besides the microstructural attributes, an ideal numerical model for the additive manufactured material should be able to consider the most crucial parameter of fatigue performance, the poor surface state which is defined by the roughness and the pores on or near the surface. Besides the establishment of a geometrical model, numerical methods involve a lot of processes, e.g. adopting constitutive models, choosing fatigue indicating parameter (FIP), post-treating simulated results, etc. A widely accepted procedure is the microstructure-sensitive modeling framework [16,17]. The framework of the microstructure sensitive modeling method for polycrystal was used successfully to reproduce the Kitagawa-Takahashi effect numerically in a wrought Stainless Steel (SS) 316L [18].

In the current study, based on the modeling framework for conventional 316L, the numerical study along with necessary experimental campaigns about HCF behavior of SLM SS 316L are presented. First, based on the Electron backscatter diffraction (EBSD) observations, geometrical models with explicit microstructure are built. From the profilometry and tomography analyses, an understanding of the inherent roughness and defects of SLM parts has been obtained. The fractography observations provide the characteristics of the fatigue-driven defects that are added to the numerical model. The outputs of finite element analysis results are post-treated by a non-local method [19] and a statistical method [20,21] in the context of fatigue prediction. Second, details about the employed numerical models are presented. The process of identification and calibration of parameters' values in both the elastic and plastic constitutive models is detailed. Third, from simulations carried out on smooth models and models with roughness and/or defects, the effects of roughness, Lack-of-Fusion (LoF) defects and microstructure are discussed based on an important number of simulation results. Considering the stress level in high cycle fatigue is low and not much plasticity is expected to develop, most of the computations are carried out using an elastic behavior. But a specific investigation regarding the effect of crystal plasticity on the prediction is conducted in a limited number of cases at last.

2. Preparatory investigations on the explicit microstructure modeling

In the numerical model proposed in the current study, several major microscopic attributes, i.e., grain morphology and grain orientation, as well as the surface state are considered. Configuration details are collected from experimental data and are presented in this section.

2.1. Grain morphology and grain size

The first challenge in explicit microstructure modeling of polycrystalline aggregate is to adequately represent the grains. The grains can be intuitively described by their shape and size which are extracted from the results of the EBSD analyses. Band Contrast (BC) is used to present the grain boundaries. BC maps of the measured areas on the X/Y plane of an SLM SS 316L sample are shown in Fig. 1. The experiments are performed at different sites of the sample used to check the consistency of the microstructural patterns at different locations of the fabricated sample. It is convenient to directly use the real microstructure. But to show the effect of each microstructural component, we need to numerically describe the microstructure and create typical representative examples. After eliminating the very small grains (equivalent grain size $D_{eq} < 2$ µm), an estimate of the average grain size can be obtained and is about 25 µm. This value serves as the average grain size in the Voronoi-polygon-tessellated finite element model. The polycrystalline aggregates are mainly constituted by large elongated grains of a quadrangle shape. Thus, besides the Voronoi model, we build up a quadrangle-tessellated model using the same grain size as well for further comparison. In addition, to emphasize the predominant large elongated grains, we process the raw data again by filtering more small grains to consider only the pronounced large elongated grains by using the threshold that the D_{eq} is lower than 5 µm. The average grain size

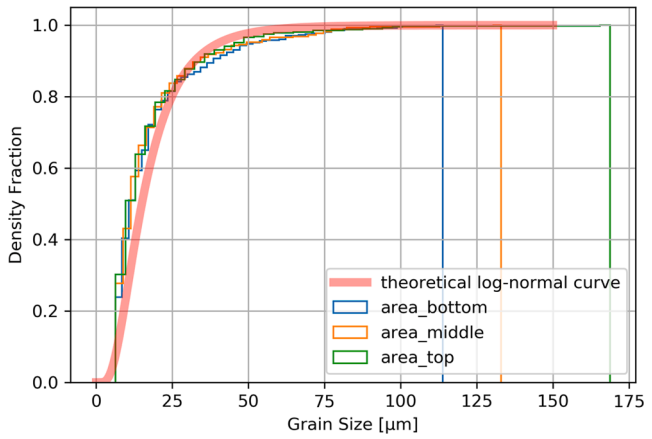

Fig. 2. Theoretical log-normal distribution and empirical distributions of grain size in an SLM SS 316L.

calculated is such that D_{eq} equals 54 μm. The ellipse approximation process provides that the average aspect ratio of the elongated grain is about 3. However, in the above-mentioned models, grain sizes are almost homogeneous. We adopt another realization of virtual microstructure by using log-normal distributed Voronoi polygon to better characterize the inhomogeneous grain morphology. The parameters of the log-normal probability distribution are $\mu = 15$ μm and $\sigma = 0.6$ μm. The distribution is plotted for this set of parameters in Fig. 2 and is compared to the experimental data. A good agreement is observed.

2.2. Crystallographic orientation

EBSD returns the Euler angles for every grain detected in the sample. In the modeling of polycrystal aggregate, a set of crystallographic orientations should be assigned to the grains. Nevertheless, our numerical model shows a virtual microstructure i.e., we create the microstructure with randomness to simulate more different configurations. If we arbitrarily assign orientations to the grains in numerical models by using the thousands of crystallographic orientations from EBSD directly, there will be a risk that we overemphasize the influence of small grains while lowering the dominant role of large elongated grains. An alternative is proposed hereby to avoid the misassignment. We duplicate the measured orientations according to the sizes of the grains where they belong to. Then, random sampling is carried out from the generated orientation set. Hence, the characteristic textured grain orientations set is obtained.

Besides the realistic textured grain orientations set, isotropically distributed grain orientation is used in the simulations as a reference to show the effect of the textured microstructure of AM material. For the isotropically distributed grain orientation set, the crystallographic orientation has no preferential direction. Hence, the orientations are homogeneously distributed in the 3D space. The isotopically distributed grain orientation sets used in this study are generated using the software Neper [22].

To present the distribution of orientations in isotropic and realistic configurations, pole figures and original EBSD data are shown in Fig. 3.

2.3. Surface roughness & defects

Roughness measurement using profilometry technique has been carried out before the numerical investigation. An SLM SS 316L of which the scanned surface has a size of 6 * 10 mm^2 was measured. The resolution of the scanner (Alicona InfiniteFocusL) was 2 μm. After filtering the data near the border of the sample that often show greater measuring errors, we have 2731 2D roughness profiles which are discretized according to the Y coordinate. Considering the 2D numerical model has a length of 5 mm, we cut the profiles at the two ends and only keep the middle parts. The standard for choosing the profile which can represent the surface features is hard to decide as the typical representative parameter to characterize the influence of surface roughness on fatigue performance is still in dispute. The most commonly used parameter is the arithmetical mean deviation (R_a). Also, there are more proposed parameters, i.e., root mean squared (Rq), maximum valley depth (Rv), maximum peak height (Rp), maximum height (Rt), skewness (Rsk), kurtosis (Rku) and mean depth from Japanese industrial standard ($RzJIS$). Because Ra is the most widely accepted roughness parameter in industrial and academic domains, we use it as the primary parameter and take into account other parameters as well. The ideal profiles should

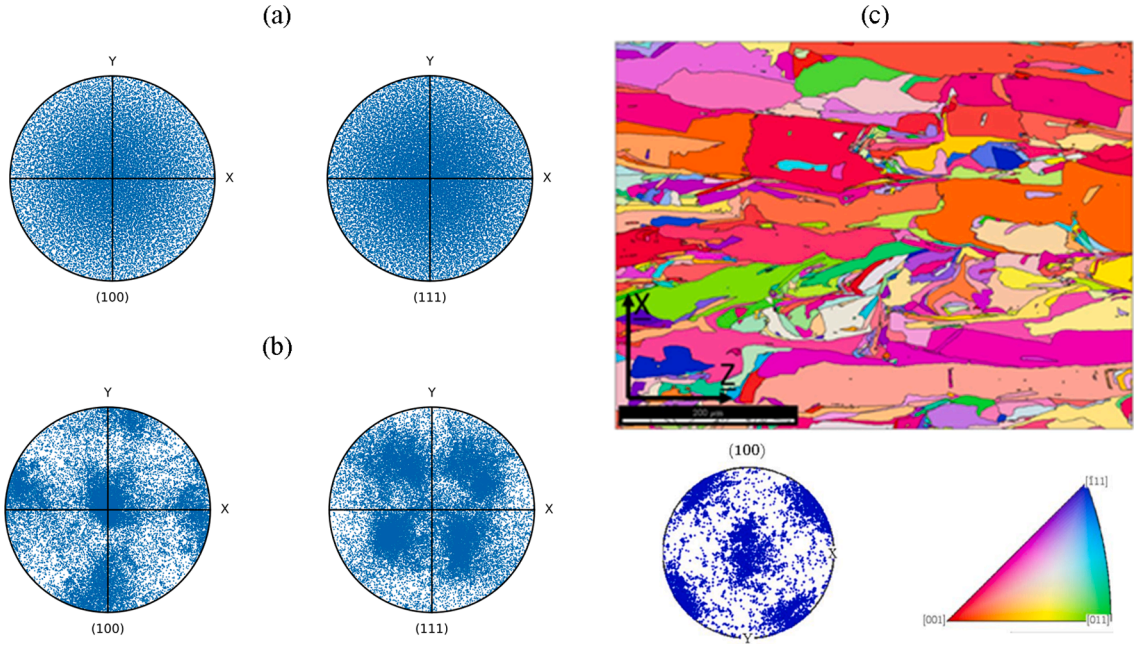

Fig. 3. Pole figures in direction 100, and 111 of employed orientation sets of (a) isotropically distributed crystallographic orientations; (b) realistic distributed crystallographic orientations in SLM SS 316L and (c) original EBSD results.

Table 1
Characteristic roughness parameters of the 5 selected profiles with schematic illustrations (re).

	Scanned surface	P1	P2	P3	P4	P5
Ra [μm]	7.23 ± 1.13	6.93	7.24	19.71	7.23	7.23
Rq [μm]	9.35 ± 1.51	8.65	9.59	22.01	10.83	11.16
Rv [μm]	23.0 ± 5.51	15.80	22.05	50.01	43.14	24.16
Rp [μm]	30.8 ± 7.02	26.61	37.06	20.72	42.72	63.54
Rt [μm]	69.1 ± 15.2	42.41	59.11	70.73	85.86	87.70
Rsk	0.447 ± 0.373	1.20	0.76	−1.24	0.79	2.70
Rku	3.92 ± 1.09	2.85	4.34	1.70	6.19	12.95
Rz(JIS) [μm]	53.9 ± 10.2	41.52	58.78	69.67	84.12	87.24

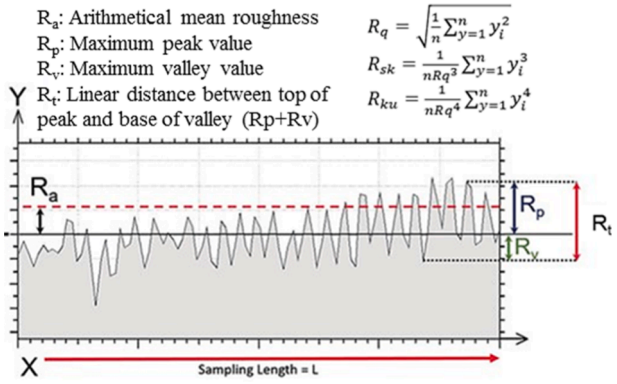

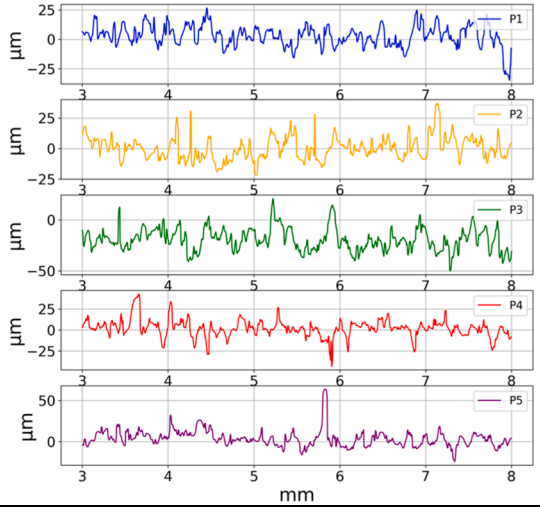

adapted from [23]

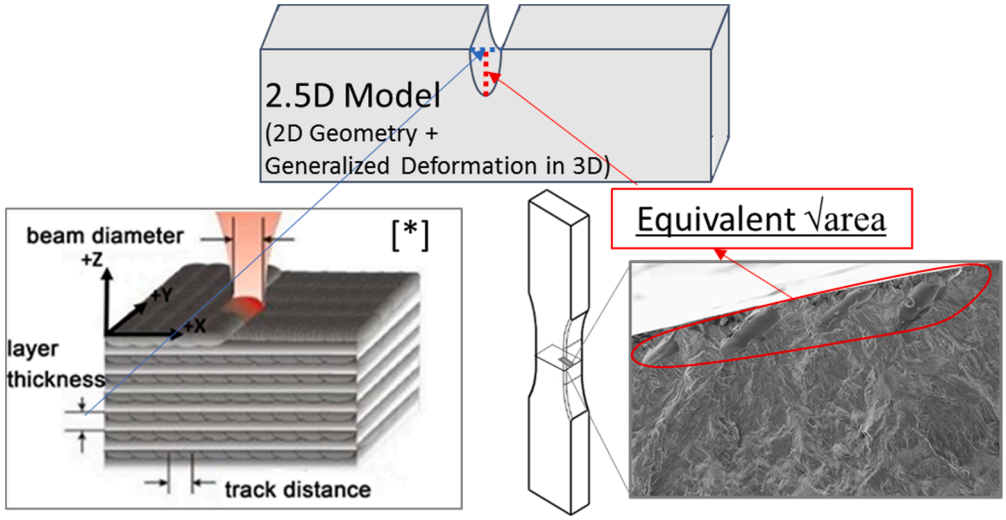

Fig. 4. Schematic illustration of designing imitating LoF defect in the numerical model (*:).
adapted from [30]

have very similar *Ra* as the whole scanned surface while the other parameters are in reasonable ranges. Profiles are chosen from different positions to prevent the similarity of geometry. The selected roughness profiles and the corresponding parameters are listed in Table 1 as well as an illustration of surface roughness parameters. P1 is the profile measured in the very middle of the specimens. Besides, P1 is relatively smooth considering its characteristic parameters. All the parameters from P2 are within one standard deviation of mean results from the whole scanned surface which makes this profile the supposed "most" representative. P3, on the contrary, is the one with parameters deviating from the references. P4 and P5 are chosen for that they have the same *Ra* values as the experimental ones. P4 has a large *Rv* while P5 has a large *Rp*. The comparison between P4 and P5 can indicate the difference between intrusion and extrusion cases. In addition, 24 additional profiles chosen by the shuffle algorithm from the scanned surface are used to keep the stochasticity of the roughness. We will compare the results from selected profiles and those from randomly chosen ones to verify whether the characteristic roughness parameters can be of value in terms of fatigue predictions.

On the fracture surfaces of the fatigue failed specimens, lack-of-fusion defects are often seen and are considered as one of the most harmful factors of crack initiation [8,10,24]. Similar observations are often obtained in previous experiments of the authors (see the right bottom of Fig. 4). This kind of defect is often undetectable by μCT or

Table 2
Configurations of the models employed in the simulations.

Tessellation			Orientation		Loading	
Name	Grain number	Average grain size [μm]	Isotropic set number	Realistic set number	Tension	Bending
*Quadrangle 1	5070	25	50	50	✓	×
*Voronoi	5070	25	50	50	✓	×
#Log-normal Voronoi 1	8400	19	24	24	✓	✓
#Log-normal Voronoi 2	8400	19	24	24	✓	✓
#Quadrangle 2	1080	54	24	24	✓	✓

*: only used in smooth models; #: used in all models.

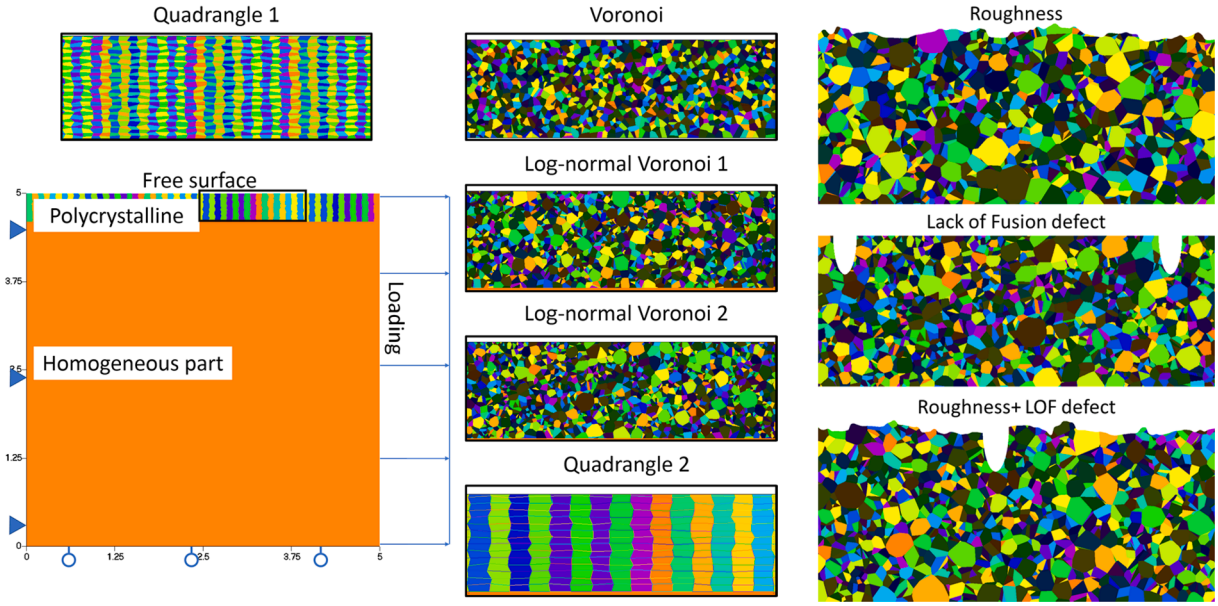

Fig. 5. Schematic illustrations of geometrical models: dimension and 5 tessellations used in the numerical model; and different types of defective models (zoom view of the local top surface).

profilometer. It should be mentioned that other surface defects such as spatter are also considered to be harmful to cyclic loading endurance [25]. However, spatter often exists as unfused powder attached to the surface and is part of the roughness profile that has been discussed in the previous section. To take the LoF defect into consideration, the estimation of an effective size from the fracture surface analyses is adopted. More exactly, we represent the 3D defects observed at the crack initiation sites by an equivalent 2D defect sharing the same Murakami parameter $\sqrt{Area}$ [26]. Previous research concerning the estimation of critical defect size can be referred [27–29]. In the current study, it is decided to use a semi-elliptical defect with a depth of 100 μm to imitate the realistic LoF defect. The observations are conducted in the transversal section while the modeling is along the longitudinal direction. The semi-minor axis representing the thickness of the LoF defect is set to 30 μm which is half of the layer thickness. Fig. 4 illustrates the way to design LoF defect in the 2.5D numerical model.

3. Explicit microstructure finite element model configurations

3.1. Design of geometrical models

Smooth models containing explicit microstructure attributes are built up to demonstrate the effect of grain morphology and grain orientations. Five tessellations are used to compare different grain morphologies. Two types of grain orientation are used. The details of each model configuration are listed in Table 2. Quadrangle tessellation 1 and Voronoi tessellation are purely based on the approximate estimation of grain size. Two extra log-normal Voronoi tessellations are used to imitate the realistic microstructure. Quadrangle tessellation 2 is added to emphasize the influence of elongated grains. The selection of morphology parameters for the latter three tessellations has been explained in the previous section. Several tens of sets of grain orientations are employed. Half are isotropically distributed and half are realistic. Both tension and bending loading conditions are applied.

The models with semi-ellipsoidal defects are designed to simulate the effect of LoF defects. As previously mentioned, equivalent 2D defects are introduced in the models to reflect the role of LoF defects. Same microstructures as the ones of the smooth models are used, as listed in Table 2 with a mark "#". The selected five roughness profiles discussed previously are added to the smooth models by geometrical Boolean operations. The models are approximations of as-built SLM sample lateral projections. Likewise, the detailed configurations are listed in Table 2 with a mark "#". The as-built samples show not only significant roughness but also LoF defects. The models with roughness and geometrical defects aim at taking both detrimental factors into considerations. All other microstructural configurations are kept the same. Schematic pictures of the geometrical models mentioned above are presented in Fig. 5.

Meshes are generated by the software Gmsh [31]. For the polycrystal part, a characteristic length of 2 μm is used in the upper half creating a very fine mesh. In the lower half, mesh size is set to 10 μm. A coarse mesh with a size of 100 μm is used for the homogenous part.

Table 3
Isotropic elastic and cubic constitutive models' parameters for the studied 316L steel with regards to the different texture configuration.

Isotropic elasticity			Cubic elasticity			
	E [MPa]	ν	C_{1111} (GPa)	C_{1122} (GPa)	C_{1212} (GPa)	anisotropic factor $2*C_{1212}/(C_{1111}-C_{1122})$
Isotropic (Non-textured)	194,000	0.284	197	125	122	3.64
Realistic (Textured)	145,100	0.330				

Table 4
Identified parameters of the Méric&Cailletaud crystal plasticity constitutive model.

C_{1111} [GPa]	C_{1122} [GPa]	C_{1212} [GPa]	K [MPa.s1/n]	m	
197	125	122	10	10	
r_0 [MPa]	Q [MPa]	B	a [MPa]	d	
83.8	5.30	1.44	2.18E5	2.61E3	
h0	h1	h2	h3	h4	h5
1	1	0.438	77.2	4.31	2.41

3.2. Constitutive models

3.2.1. Calibration of parameters in the elastic constitutive model

The material constitutive equations used in the current simulations are of three types: isotropic elasticity, cubic elasticity and crystal plasticity. Regarding cubic elasticity, the values of C_{1111}, C_{1122}, and C_{1212} are the ones of γ-Fe [32]. For the case of isotropic elasticity, a detailed discussion is presented. As the finite element model is composed of one homogeneous part and one polycrystal part, isotropic elasticity is attributed to the homogeneous part. The aim of calibrating the isotropic elastic model is to make the homogeneous part consistent with the polycrystal part. Since the cubic elastic parameters C_{1111}, C_{1122} and C_{1212} have been determined, Young's modulus and Poisson ratio are calibrated considering the macroscopic responses of a polycrystalline aggregate containing numerous grains. It should be noted that two sets of parameters' values in isotropic elasticity are used. The parameters are calibrated by a model with isotropically distributed grain orientations and a model with textured microstructure. Values for the parameters of the two elastic constitutive models are listed in Table 3.

3.2.2. Identification of parameters in polycrystal plastic model

A phenomenological crystal visco-plasticity model proposed by Meric et al. [33] is used. The plastic slip velocity of every system follows a Norton type visco-plastic flow law

$$\dot{\gamma}_s = \left\langle \frac{|\tau_s - x_s| - r_s}{K} \right\rangle_+^n sign(\tau_s - x_s) \tag{1}$$

where

$$sign(y) = \begin{cases} -1 & if \quad y < 0 \\ 0 & if \quad y = 0 \\ 1 & if \quad y > 0 \end{cases}$$

$$\langle y \rangle_+ = \max(y, 0) \tag{2}$$

and K and n are viscosity parameters. x_s and r_s are the kinematic hardening variable and the isotropic hardening variable on the slip system denoted by s, respectively.

$$x_s = c\alpha_s \quad and \quad \dot{\alpha}_s = \dot{\gamma}_s - d\dot{v}_s\alpha_s \tag{3}$$

where c and d are material parameters.

$$r_s = r_0 + Q\sum_{r=1}^{12} h_{sr}[1 - \exp(-bv_r)] \quad and \quad \dot{v}_r = \left|\dot{\gamma}_r\right| \tag{4}$$

where r_0 is the initial critical shear stress and b is a coefficient of material sensitivity to saturation and h_{sr} is an interaction matrix.

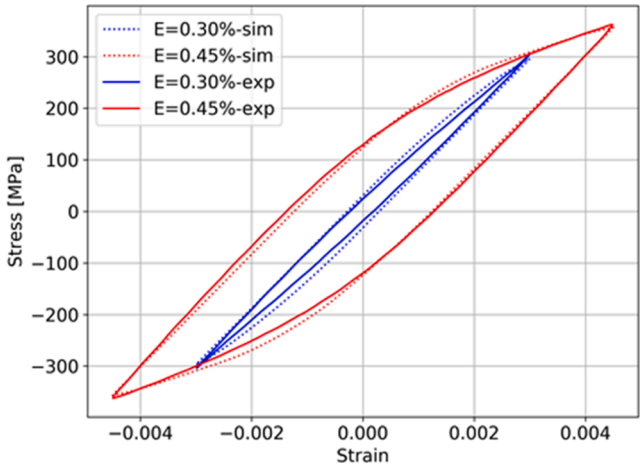

Fig. 6. Comparison between the experimental responses of 316L steel under different imposed amplitudes and the predictions of the crystal plasticity model.

The identification of the crystal plasticity constitutive model is based on previous cyclic tension-compression experiments of an SLM SS 316L at the loading levels of $\varepsilon = 0.3\%$ and $\varepsilon = 0.45\%$. Data were collected at the half-life cycle. A self-consistent model rather than a finite element method or spectral method is used as the identification methodology because of its efficiency in calculation of macroscopic fields [34]. The NSGA II algorithm [35] is employed as the optimization algorithm. The identified parameters of the crystal plasticity constitutive model are listed in Table 4. Comparisons between simulations and experiments are plotted in Fig. 6. The identified parameters yield stress-strain curves in good agreement with the experimental ones.

3.3. Loading condition

The present simulations involve two loading modes: cyclic bending and cyclic tension. The loading ratio is always −1. Regarding the elastic models, the stress amplitude is arbitrarily set to 100 MPa since all generated responses are linear. Results are linearly transformed in post-treatment. The stress amplitudes for plastic models are decided by the estimation of macroscopic fatigue limits which are dependent on the model configurations. The values are presented afterward along with the analyses of results.

3.4. Fatigue criterion

A stress-based fatigue criterion, the Dang Van criterion [36] is used to estimate the fatigue crack initiation. In the Dang van criterion, there are two parameters involved in the fatigue process, namely the microscopic shear stress in grain area and the microscopic hydrostatic stress, both assessed in the elastic shakedown state. The former is responsible for crack nucleation along with slip bands and the latter influences the crack opening process. This criterion is mathematically formulated as follows:

$$\max_t \left\{ \max_{\underline{n}} \left[\|\underline{\widehat{\tau}}(\underline{n}, t)\| + \alpha_{dv}\widehat{\sigma}_{hyd}(t) \right] \right\} \leq \beta_{dv} \tag{5}$$

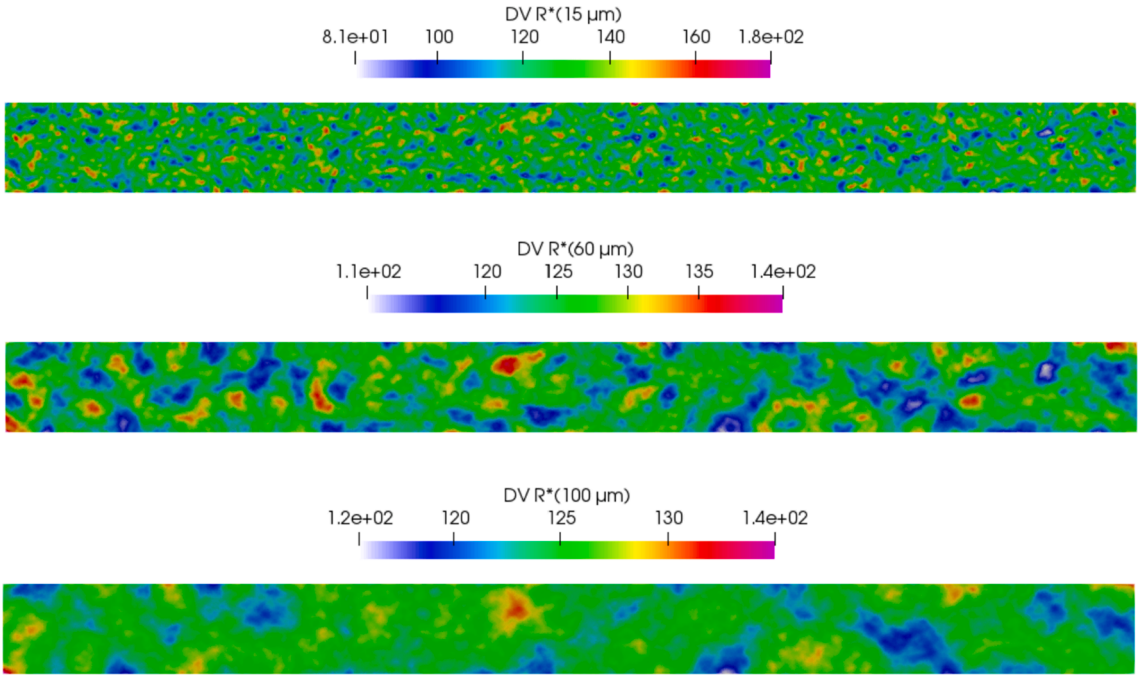

Fig. 7. Dang Van stress distributions with respect to different non-local parameters in one smooth polycrystal model subjected to a tension loading of 100 MPa.

In which, $\widehat{\tau}_{-}$ denotes resolved shear stress and $\widehat{\sigma}_{hyd}$ denotes hydrostatic stress. As the cyclic loading changes with time, both $\widehat{\tau}_{-}$ and $\widehat{\sigma}_{hyd}$ are time-dependent and are expressed as functions. n_{-} is the slip systems in a grain. α_{dv} and β_{dv} are material parameters identified from tension and torsion fatigue limit (s_{-1} and t_{-1}) by following equations:

$$\alpha_{dv} = \frac{t_{-1} - \frac{s_{-1}}{2}}{\frac{s_{-1}}{3}}; \quad \beta_{dv} = t_{-1} \tag{6}$$

There are more stress-based fatigue criteria in the literature [37,38]. Previous research shows that in the case with a simple loading condition, the yielded results will not be sensitive to the criteria [39].

3.5. Discussion on the experimental reference for fatigue simulation

Since the geometrical model has been thoroughly described before, one of the remaining questions is how to decide the reference fatigue limit for future comparisons.

In the literature, the reported fatigue limits of SLM SS 316L are not always consistent. One consensus is that fatigue performance is strongly dependent on the fabrication and post-processing processes. The characteristics of the microstructure are not always available in the reported investigations of the literature. Moreover, torsional fatigue tests of SLM 316L are rarely mentioned in the literature while the torsional fatigue limit is essential to calibrate the parameters in fatigue criteria. Material constants α and β in the stress criteria are deduced from both the tension

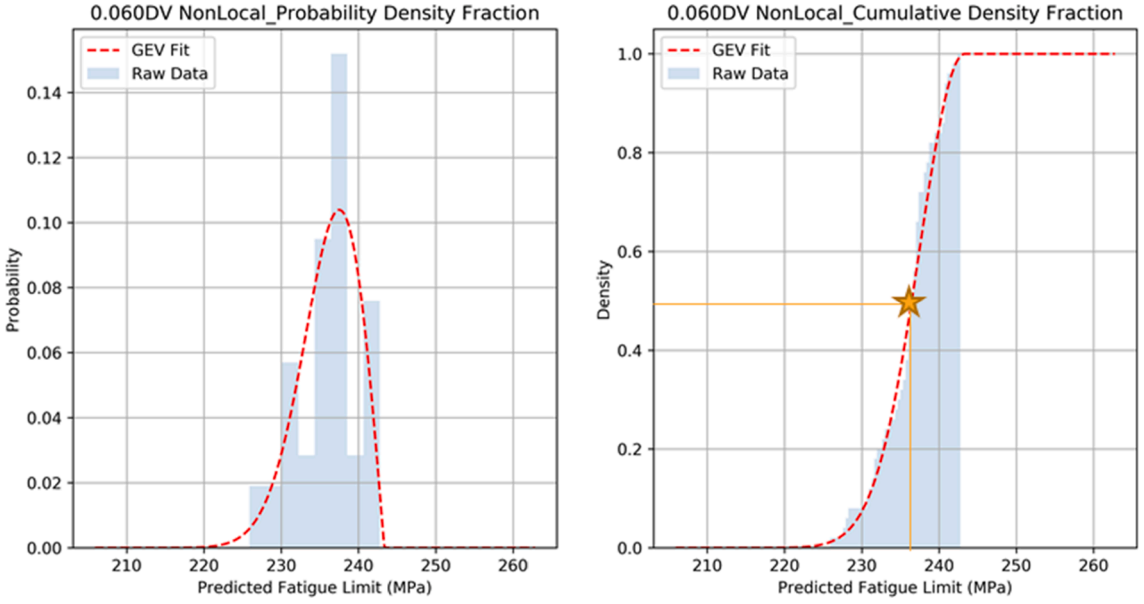

Fig. 8. Probability density fraction and cumulative density fraction curves fitting the stochastic responses of FIP in polycrystal models with different microstructural configurations using R* = 60 μm.

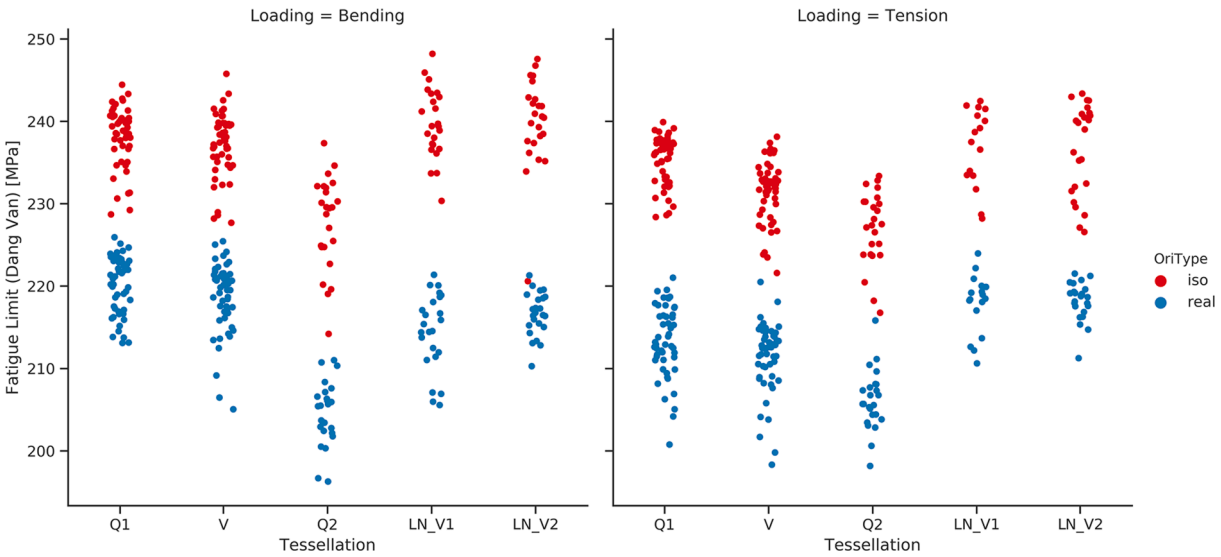

Fig. 9. Scattered predicted fatigue limits from Dang Van criterion (with R* = 60 μm) regarding texture types and categorized by the tessellation type.

fatigue tests and the torsion fatigue tests. Therefore, finding the referential fatigue limits of SLM SS 316L from the literature seems to be unachievable at the moment.

Because the torsion fatigue limit is an indispensable parameter in the adopted fatigue criterion and. the authors prefer to use experimental data from one researcher for consistency. Eventually, the fatigue limits used to calibrate the simulations for the SLM SS 316L are 230 MPa in tension-compression loading with a ratio of −1 and 147 MPa in fully reversed torsion, respectively. These values are from the previous research on a wrought SS 316L [40]. In the study of Riemer et al. [11], the fatigue limit of SLM SS 316L is in the range of 250–280 MPa under bending loading. Elangeswaran et al. reported a fatigue limit of the same order for HIPed SLM 316L under tension-compression loading [41]. Hence, using 230 MPa as the fatigue limit s_{-1} seems to be a reasonable choice. Furthermore, the current numerical investigations are performed mostly under the cubic elastic constitutive model in which the responses can be changed proportionally. In other words, the tendencies observed from our simulations should remain valid even though the reference limit is different.

With the fatigue limits chosen, the values of parameters mentioned in the adopted criterion are deducted: $\alpha_{dv} = 0.403$ and $\beta_{dv} = 147$ MPa.

4. HCF simulation results from elastic constitutive models

4.1. Smooth models

A comprehensive study dealing with the statistical assessment of the fatigue strength dispersion of pure copper is reported in the literature in which generalized extreme value (GEV) distribution is applied on a mesoscopic scale to describe the extreme essence of fatigue phenomenon [20]. Details on the GEV theory can be found in [42–44]. This microstructure-sensitive modeling framework is employed with adaptation in this study to deal with the stochasticity in the configurations of the microstructural attributes as well as the surface state. Instead of restraining on a one-grain-scale, the investigation is expanded to the whole numerical model by introducing the non-local method.

The non-local approach using integration over a sphere/circle of critical radius R* can be referred to [18]. As shown in Fig. 7, we test 3 different values of R*: 15 μm, 60 μm and 100 μm. The loading mode is tension. The distribution of averaged FIP (Dang Van stress in this case) is presented. The parameter β_{DV} equals 147 MPa which is the torsional fatigue limit for wrought 316L. The effective zone with a radius of 15 μm yields a maximum Dang Van stress of about 180 MPa which implies a fatigue limit of about 190 MPa. This value is considered to overemphasize the effect of stress heterogeneity. The prediction of fatigue limit (240 MPa) from R* equating to 60 μm is higher than the experimental result (230 MPa). As the previous prediction is from one single model, we conduct simulations with 50 different isotropically distributed orientation sets then fit the response with Weibull distribution (Fig. 8). Based on the assumption that the critical fatigue limit is the value at which 50% of the cracks initiate, we use the median value of the GEV fitted data to represent the predicted fatigue limit. The predicted fatigue limit from the benchmark models is 236 MPa. The interval of 95% confidence is from 228 to 242 MPa. The simulations have hence a good agreement with the experimental results when R* = 60 μm is applied.

The fatigue limit predictions using R* = 60 μm from Dang Van criterion for the smooth models are plotted for different loading modes, orientations and tessellations (see Fig. 9). The difference between the two orientation types is noticeable while the effect of loading mode is negligible. The models with isotropically distributed orientations yield predictions in the range from 220 to 250 MPa which is consistent with the conventional fatigue limit. The models containing orientations collected from AM specimens have obvious weaker performances. The median values of predicted fatigue limits from models with the same type of loading, tessellation and orientation are calculated. The data are

Table 5
Median values of predicted fatigue limits from models with the same type of loading, tessellation and orientation using non-local Dang Van criterion (R* = 60 μm).

	Bending			Tension		
Tessellation	Isotropic	Realistic	Difference [%]	Isotropic	Realistic	Difference [%]
Q1	239	221	7.6	236	213	9.8
V	238	220	7.6	232	212	8.5
Q2	230	205	10.5	227	206	9.6
LN_V1	239	215	10.2	238	218	8.2
LN_V2	241	217	9.9	239	219	8.6

Table 6
Median values of predicted fatigue limits from models with the same type of loading, tessellation and orientation using Dang Van criterion with different values of R*

R* [μm]		Bending			Tension		
	Tessellation	Isotropic	Realistic	Difference [%]	Isotropic	Realistic	Difference [%]
15	Q2	192	169	12.4	187	165	12.0
	LN_V1	203	180	11.2	204	180	11.7
	LN_V2	202	182	9.9	200	180	10.0
30	Q2	210	186	11.5	208	183	11.7
	LN_V1	219	197	10.3	223	201	10.1
	LN_V2	221	201	9.4	221	201	9.2
45	Q2	219	196	10.8	220	197	10.5
	LN_V1	230	207	10.0	232	211	8.9
	LN_V2	235	211	10.3	232	212	8.7
60	Q2	230	205	10.5	227	206	9.6
	LN_V1	239	215	10.2	238	218	8.2
	LN_V2	241	217	9.9	239	219	8.6

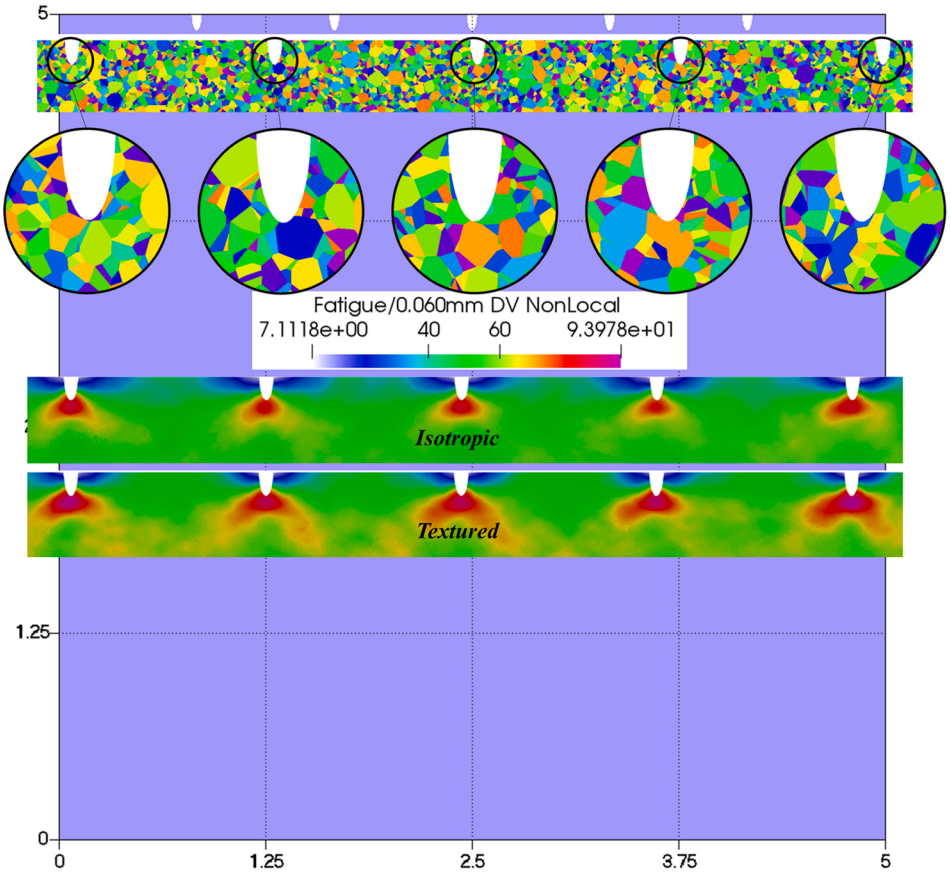

Fig. 10. Distributions of the non-local fatigue indicating parameters (Dang Van (R* = 60 μm)) in non-textured and textured numerical models under tension loading of 100 MPa.

listed in Table 5. It can be concluded that the realistic texture can lead to a drop in the predicted fatigue limit of around 10%. It is noteworthy that the average grain size of each batch is not equivalent. But the yielded results are close to each other.

Even though R* is always set to 60 μm in the previous analyses, we cannot state it is the correct value to be used. More differently configured experiments and simulations will be needed to validate or refute the current choice. So far, this value of R* yields possible comparisons with experimental data and provides some qualitative findings with respect to the effect of microstructure. The results reached with other values of R* using the Dang Van criterion are listed in Table 6. The effect of grain orientation is slightly higher when using a small R* but it remains close (variation of 2% at most). Hence, the differences observed due to the textures are consistent regardless of the non-local parameter, grain morphology or loading mode.

4.2. *Models with artificial semi-ellipsoidal defects*

The models with artificial semi-ellipsoidal defects are imitations of SLM specimens containing notable LoF defects. Let us recall that the numerical models do not keep the exact geometries as the 3D realistic defects are transferred to 2D and their shape complexity is simplified.

Fig. 10 shows the distributions of the FIP using the non-local method together with the Dang Van criterion. One model is attributed to isotropic crystallographic orientations while the other one has a realistic textured microstructure as in the SLM steel. Considering the critical radius method, R* is set to 60 μm which is consistent with the value used for smooth models in previous simulations. On one hand, the responses

Table 7
Mean values of predicted fatigue limits from models containing geometrical defects with the same type of loading, tessellation and orientation using non-local Dang Van criterion (R* = 60 μm).

Configuration ("Tessellation", "Orientation", "Loading")	Smooth Model [MPa]	Model with defect [MPa]	Drop of fatigue limit [MPa] ([%])
('LN_V1', 'Realistic', 'Bending')	215	161	54 (25%)
('LN_V2', 'Realistic', 'Bending')	217	160	57 (26%)
('Q2', 'Realistic', 'Bending')	205	159	46 (22%)
('LN_V1', 'Isotropic', 'Bending')	239	174	65 (27%)
('LN_V2', 'Isotropic', 'Bending')	241	175	66 (27%)
('Q2', 'Isotropic', 'Bending')	230	172	58 (25%)
('LN_V1', 'Realistic', 'Tension')	218	156	62 (28%)
('LN_V2', 'Realistic', 'Tension')	219	156	63 (29%)
('Q2', 'Realistic', 'Tension')	206	156	50 (24%)
Wrought 316L (artificial defect introduced) [40]	230	180	50(22%)
SLM 316L (polished vs as-built) [7]	150	100	50(33%)

from the textured model are higher compared to that of the isotropic model which demonstrates the effect of grain orientation. On the other hand, although the hot spots are always in the defect root, their forms are dissimilar, especially for the textured model. The crystallographic texture changes the distribution of Dang Van stress. This phenomenon is emphasized in the textured case.

To keep results consistent, R* is set to 60 μm for both the smooth models and the models with pores. The average values of the predictions are listed in Table 7. From the table, the added artificial defects result in a decrease of about 25% for all the configurations. Considering the limited numbers of experiments leading to uncertainty regarding the actual fatigue limit of AM 316L, the differences between experiments and simulations are acceptable. The effect of crystallographic texture can be highlighted by comparing the two grain orientation sets. The differences are around 10 MPa. The bending loading and the tension loading lead to negligible differences.

4.3. Models with roughness

Fig. 11 shows the non-local Dang Van stresses using different R*, namely 15, 30, 45 and 60 μm, for a log-normal Voronoi-polygon-tessellated model with roughness. If a small effective zone is considered, i.e., R* equals 15 μm, the effect of stress concentration is emphasized. The hotspot always emerges in a groove of the roughness. As the R* increases, the critical position is found to move from the root of the surface defect to the grain boundaries. The hot spot shift is due to the competition between roughness and microstructure. In the defect root, stress concentration is strong, but the affected area is dependent on the defect size. Considering the roughness of SLM material, the *Ra* is often of about 10–20 μm. Therefore, the highly stressed zone is small in size. The grain boundaries, however, experience heterogeneous load levels from the local texture. Though the stress increase due to the neighboring grain effect is not as strong as the stress concentration in defect root in terms of amplitude, the related distributions are quite different. The results from 4 different R* values show that the effect of roughness is more pronounced by using a smaller R* value while the effect of microstructure (texture in this case) overwhelms the effect of roughness with a larger R* value.

The above analysis shows the details of just one model from the perspectives of non-local methods and fatigue criteria. For the selected profiles, a series of statistical analyses are conducted. Roughness profile P2 is considered as the most representative one for the reasons explained previously. Simulated results from models using this profile are firstly analyzed. The predictions using Dang Van criterion are fitted by the GEV distribution and are plotted in Fig. 12. The solid lines represent predictions of critical radius method while the dashed lines illustrate the yielded values of the neighbor layer method. Histograms of raw data are provided by the semi-transparent contours of the side-by-side bars. Scatters can be seen in every group because of the stochastic microstructure. It is observed that the larger the non-local parameters, the lower the scatter. Considering the predictions, it is difficult to decide which non-local parameters are the most appropriate since no experimental results can be used as a reference. We may only offer some conjectures knowing the roughness has a negative influence on fatigue performance. And for the case in which R* = 60 μm, the predictions may underestimate the danger of roughness.

The predictions from the 5 selected profiles are plotted in a bar chart (see Fig. 13). By comparing the selected profiles, several findings can be obtained. First of all, most of the results from these profiles are quantitatively approximate. Considering the profile P1 which is selected because of its unique position (in the middle) as well as its smoothness, the predictions are always the highest. About the profile P2 who fits the metrics best, the predictions are always intermediate. Profiles P4 and P5 are chosen because their *Ra* are identical. P4 shows a high *Rv* meaning a large maximum valley depth, whilst P5 has a high *Rp* meaning a large maximum peak value. It seems that the concave defect is more harmful

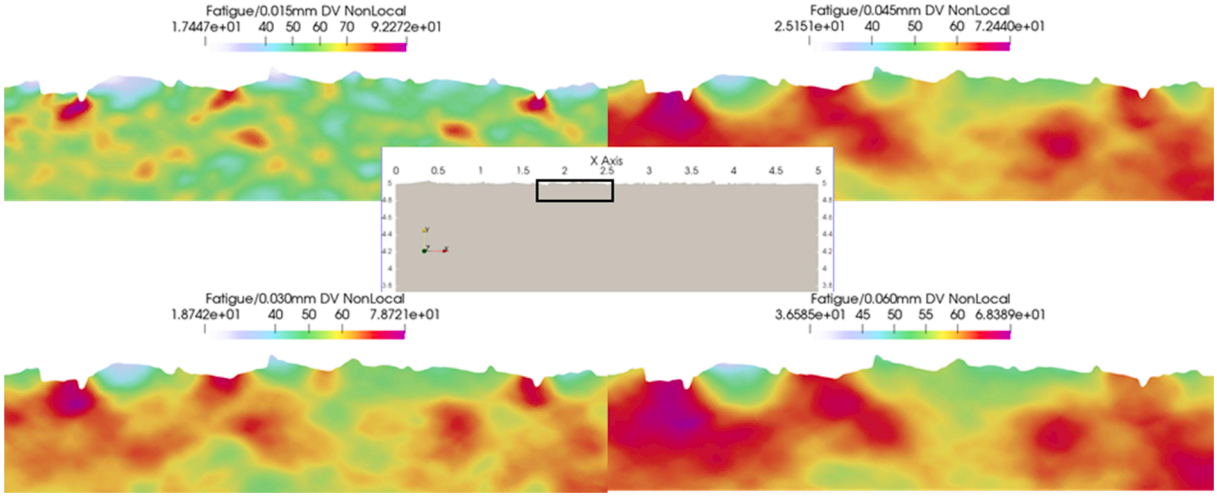

Fig. 11. Non-local Dang Van stresses using different R* (15, 30, 45 and 60 μm) for a log-normal Voronoi-polygon-tessellated model with roughness.

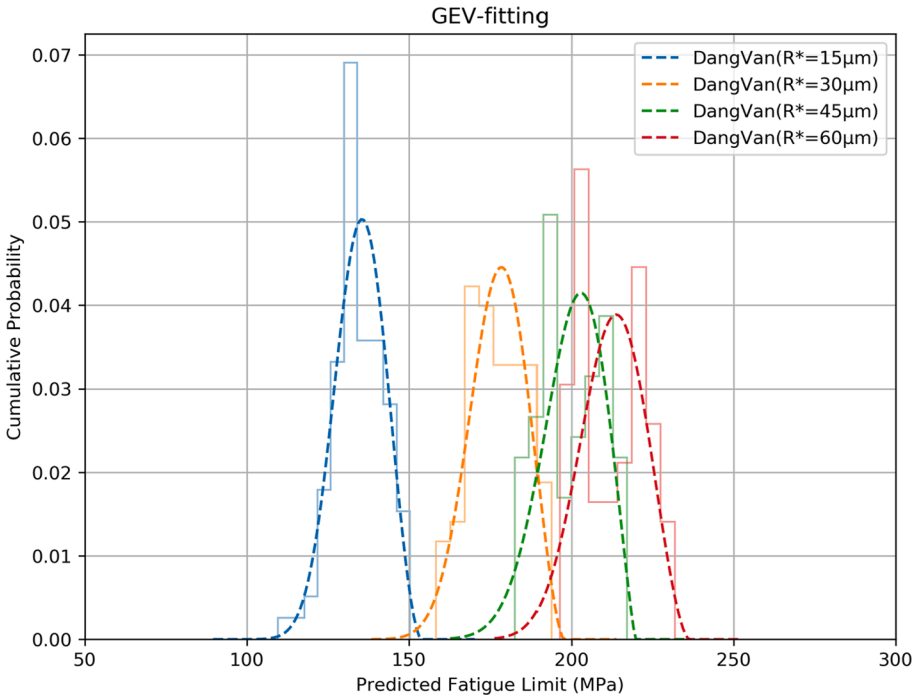

Fig. 12. Histograms and fitted Weibull distribution curves of predicted fatigue limits using different non-local parameter values for stochastic configured polycrystal models. The studied roughness profile is P2 while the crystallographic orientations are arbitrary.

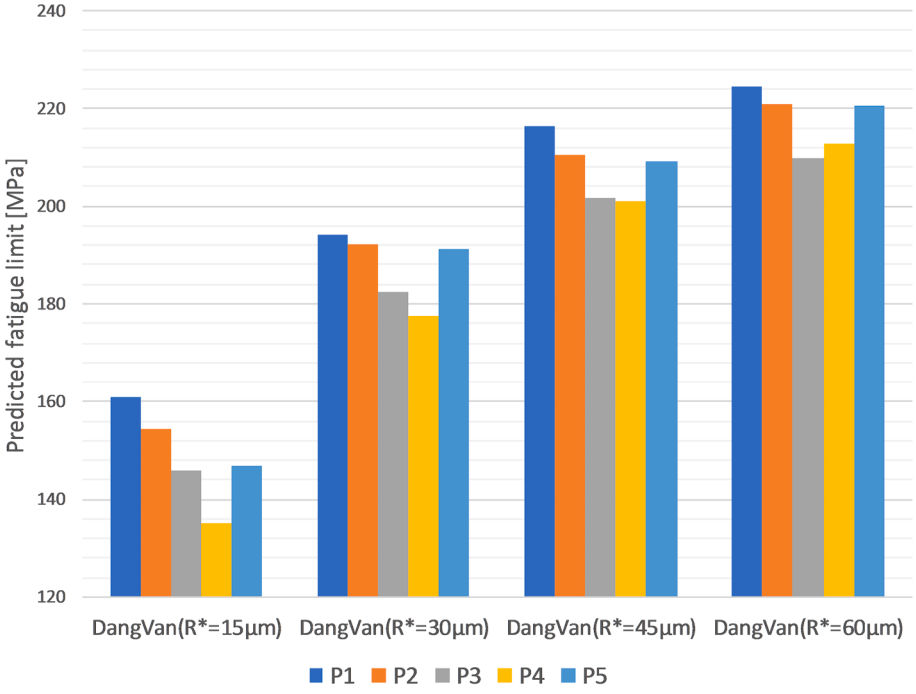

Fig. 13. Medium values of predicted fatigue limits using different non-local FIPs with respect to different roughness profiles.

than the convex defect since the results from P4 are always lower than the ones from P5. P3 is a profile noticeably rougher than the others. However, the lowest fatigue strengths are not always from P3. Except for the cases where R* = 60 μm, the most conservative predictions are attributed to P4. But comparing the *Rv* of 50 μm from P3 and of 43 μm from P4, it is found that P3 has a higher maximum valley depth.

It seems that the predicted fatigue performance cannot be directly linked to the metrics of roughness. To better explore the relationship between the fatigue performance and the surface roughness, results from the 24 randomly chosen profiles are also taken into consideration. In Fig. 14, the predicted fatigue limits versus their corresponding roughness metrics are plotted. Each point refers to the average value of 96 instantiations constituted by 48 crystallographic orientations in 2 differently tessellated polycrystal models using the same roughness profile. The investigated roughness metrics are *Ra*, *Rq*, *Rv* and *Rt*. *Ra* and *Rq* which describe the surface status globally do not present an evident correlation with the fatigue limit predictions. *Rv* which indicates the local extreme situation, as expected, seems to have an evident negative

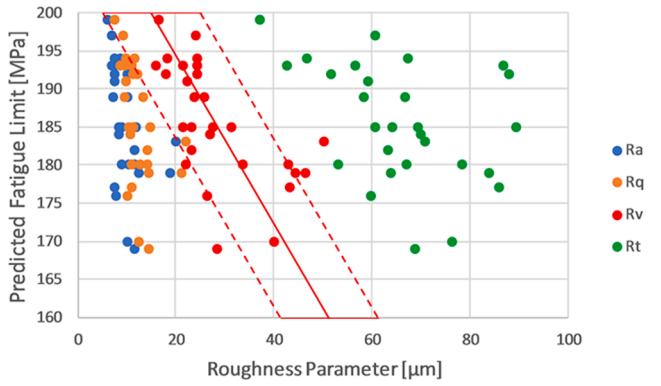

Fig. 14. Predicted fatigue limit (using non-local Dang Van with R* = 30 µm) of models containing surface roughness versus roughness characteristic parameters.

correlation with the predicted fatigue limits. Likewise, *Rt* shows a similar tendency with *Rv* while the scatter of results is stronger. Considering that Rt is the sum of *Rv* and *Rp*, it can be implied that *Rt* and *Rv* are closely related.

This part focuses on the relation between the surface roughness state and the corresponding fatigue strength. The current investigation reveals that the characteristic parameters of roughness have certain relevance with fatigue performance. But a direct connection between fatigue strength and one or several roughness parameters cannot be found. Proposing a new fatigue-describing roughness characteristic parameter requires more further in-depth study and is out of the scope of the current project. The simulation approach built in this study can nonetheless be a useful tool to carry out such an investigation.

Modeling the surface roughness effect on HCF strength for SLM Ti6Al4V from surface topology has been investigated by Vayssette et al. [45]. In their study, homogeneous behavior has been used for the first approximation. In the present study, models with explicit microstructure using an anisotropic behavior presents the scatter of responses as can be seen in Fig. 13. Although direct comparison cannot be made since the studied material is not the same as well as the numerical model is differently organized, one can still notice that considering the roughness explicitly in the numerical model quantitatively reflects the stress concentration state in the free surface. Besides, using non-local parameter provides a solution to connect the local mechanical response and the overall fatigue failure.

4.4. *Models containing artificial defect and roughness*

According to the experimental findings, the effect of the LoF defect is assumed to be much more detrimental than the effect of roughness since the polishing procedure does not improve significantly the fatigue strength [7]. A batch of models containing both artificial defects imitating LoF defect and roughness are built up. Finite element analyses and fatigue post-treatments are performed. Via comparison to the previous findings from models with defects only and models with roughness only, the results are expected to provide some qualitative understandings about the differences introduced by the defect and the roughness.

Fig. 15 shows the distributions of FIP (Dang Van stress) of models with the same microstructure configurations (morphology and orientation of grain). To better present the effect of roughness, R* is set to 30 µm. As explained in the previous section, an intermediate R* value seems to be logical for the current scale of roughness. For the model with roughness only, the groove in the roughness profile yields an extreme response for the prediction. However, in Fig. 15(c), the defect roots

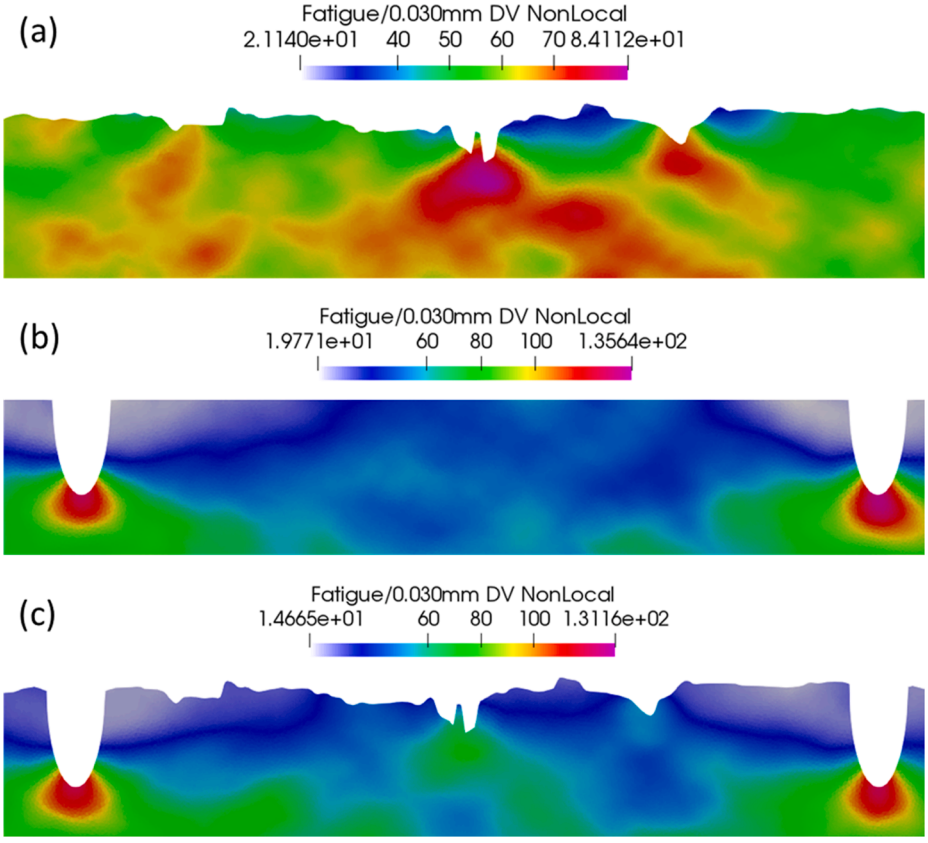

Fig. 15. Distributions of FIP (non-local Dang Van stress with R* = 30 µm) of models with the same microstructure configurations (morphology and orientation of grain) but different defect(s): (a) surface roughness, (b) LoF defects, (c) surface roughness + LoF defects.

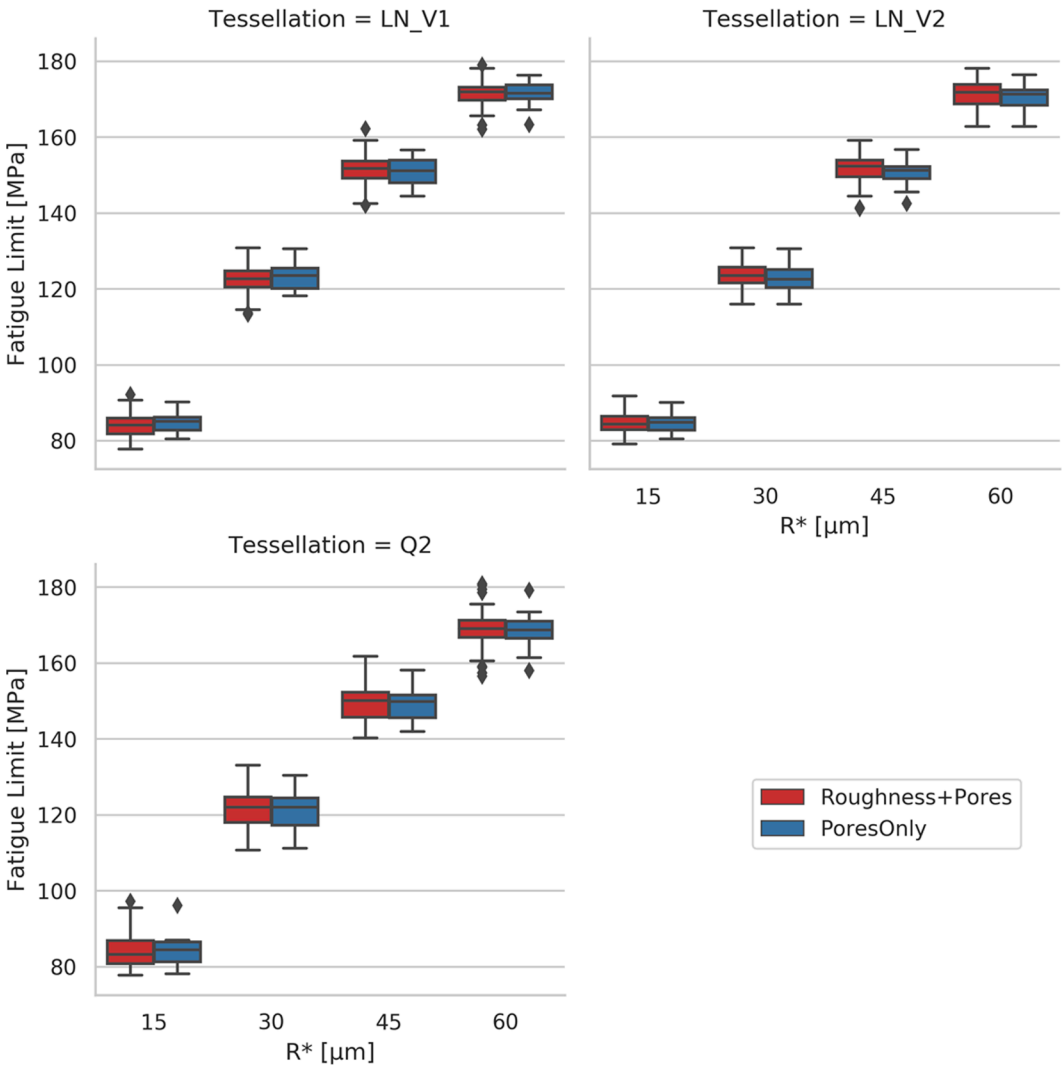

Fig. 16. Predictions of fatigue limit from Dang Van criterion using different values of R* categorized by the tessellation type (2 log-normal distributed Voronoi tessellations: LN_V1, LN_V2 and 1 quadrangle tessellation: Q2).

generate much higher FIP values. Moreover, the maximum value of FIP in Fig. 15(c) turns out to be even a bit lower than that in Fig. 15(b) which leads to a counterintuitive conclusion that the roughness may result in a positive effect on fatigue strength. Anyway, it is a rare example because of the arrangement of those irregularities in the roughness profile. Generally, the high stressed areas are dominated by the introduced large LoF defects. The irregularities from roughness generate stress concentrations as well as stress relief in certain zones. To better evaluate the effect brought by roughness on the effect of large defects, more simulations are needed.

Simulations with models containing geometrical defects with or without roughness are conducted. The employed loading mode is bending. The textures of the microstructure are of a realistic type. 24 instantiations of crystallographic orientations are used. Dang Van stresses assessed from the critical radius method are categorized by the tessellation type and are shown in Fig. 16. First, none of the tessellations shows an evident difference with the other two. LN_V1 and LN_V2 are two different tessellations in terms of grain positioning. But the results from both models are similar. Even though there are fewer grains used in the Q2 tessellation, it still generates consistent results compared to the Voronoi-polygon tessellated models. Second, the comparisons between models with or without roughness demonstrate that in the tested configurations where the geometrical defect is large and the roughness is relatively small in scale, the roughness seems to be negligible. Although it cannot yet be proved by the experiments, the tendency is shown by simulations.

It may be controversial that the current simulations cannot represent the realistic condition of SLM material because it involves several conjectures about the transition from 3D to 2D, defects' shape, arrangement, etc. Nevertheless, it reveals that the effect on fatigue strength of the combination of several large defects and a series of small defects is mainly controlled by the large defects.

5. Role of plasticity in HCF simulation of SLM 316L

5.1. Comparisons between elastic and plastic constitutive models in smooth models

For the plasticity-involved models, one major challenge is to decide the loading level as the non-linearity in mechanical response raises issues in predicting the fatigue limit. To solve this problem, the only solution is to conduct iterative simulations. However, for qualitative research in this section that aims at revealing the role of plasticity in fatigue simulation, we choose only certain representative loading levels. Without loss of generality, the smooth model with isotropic texture is considered as a conventional wrought 316L whose fatigue limit has been determined in Guerchais's research [40]. The tension loading level is thus set to 230 MPa. As a comparison, the smooth model with realistic

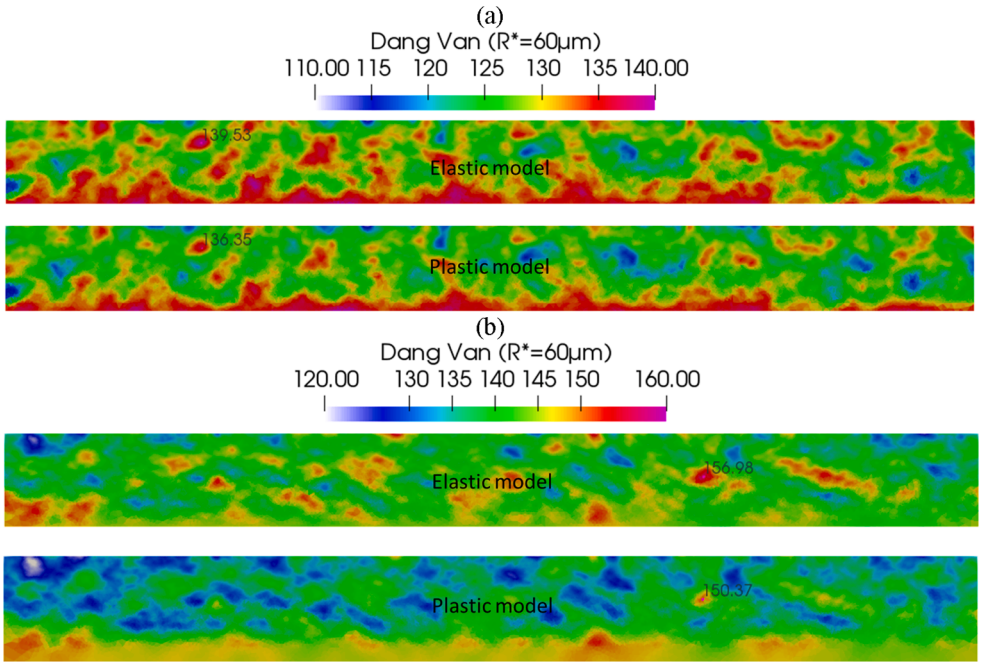

Fig. 17. Distribution of the Dang Van stress (R* = 60 μm) in smooth polycrystalline aggregates using plastic and elastic constitutive models respectively after a cyclic tension loading at 230 MPa: (a) isotropic texture; (b) realistic texture.

texture is subjected to the same loading to show the effect of grain orientation.

The first test is realized by using the smooth model with isotropic texture and realistic texture under cyclic tension loading. The geometry of the smooth model is the same as the one used in the previous section. The stabilized cycle is considered achieved in the 5th cycle. Compared to a polycrystalline aggregate with only the elastic constitutive model, the plasticity-involved model does not exhibit a remarkable difference in the distribution of von Mises equivalent stress. The distributions of FIP with the non-local method applied are shown in Fig. 17. The chosen FIP is Dang Van stress with an R* equal to 60 μm which is the same as that used in the previous section. The two constitutive models generate very similar results. It should be noted that high localization is observed at the bottom which is the interface of polycrystal part and homogeneous part. This is partly due to the neighboring effect [46]. Besides, the bottom half uses coarse meshes. Since the extreme values are still in the top half where refined meshes are used, this localization does not affect the yielded response. Comparing the responses in the same hotspot, the yielded response is 136 MPa in the plastic model while it is 140 MPa in the elastic model. The elastic model does overestimate the stress response, but the difference can be neglected when predicting fatigue failure. Similar analyses are carried out for the realistically textured smooth model which is considered as an imitation of the SLM 316L. Theoretically, the strongly textured microstructure in SLM 316L should result in a more stressed state. As can be seen from Fig. 17(b), with the added plasticity, the responses from the plastic model are lower than those from the elastic model. Due to the preferential grain orientation, the plastic deformation is more pronounced compared to that in the same model but with isotropic texture. A decrease of 4.3% in the extreme value of non-local Dang Van stress is seen, 157 MPa in the elastic model whilst it is 150 MPa in the plastic model. It should be noted that the applied loading is 232 MPa which is the fatigue limit for conventional 316L with isotropic texture. And the extreme values in both configurations exceed the threshold which indicates that the current loading is over the critical fatigue limit.

The absence of plasticity in the previous batches of simulations of smooth models does not evidently change the fidelity of results. However, with the presence of defects, the stress concentration occurs in the defective models. The role of plasticity is thus evaluated for defective models in the following section.

5.2. *Comparisons between elastic and plastic predictions in defective models*

In the previous simulations, three types of models were used: model with roughness, model with artificial defect and model with combined

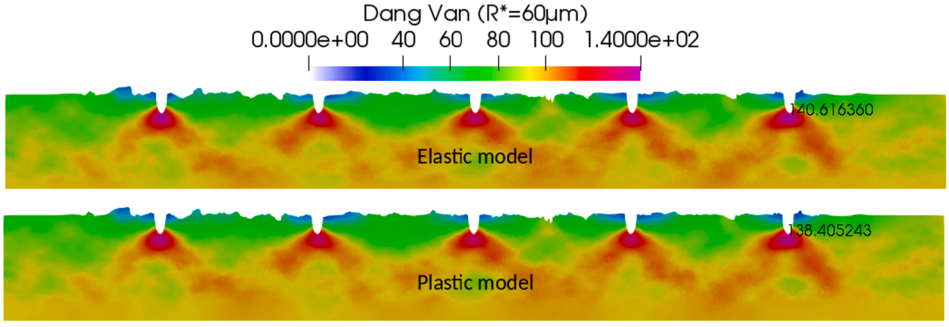

Fig. 18. Distribution of the Dang Van stress (R* = 60 μm) in defective polycrystalline aggregates using plastic and elastic constitutive models respectively with realistic texture after a cyclic tension loading at 150 MPa.

Table 8
Comparisons of predictions from a crystal plasticity model and a purely elastic model under a cyclic tension loading at 150 MPa.

Model configuration	R* (μm)		
	30	45	60
Roughness	98.8%	99.5%	99.5%
Defect	95.3%	97.8%	98.5%
Roughness + Defect	94.7%	97.0%	98.4%

roughness and artificial defect. The geometries are kept as well as the grain orientation sets. That is to say, the only change made in this batch of simulations is to change the constitutive model which allows us to check the differences brought by plasticity. Three loading levels representing the fatigue limits of as-built (with roughness and LoF defect), simple-polished (LoF defect only) and total-polished (no notable defect) bending samples are tested: 90, 120 and 150 MPa.

For the most critical configuration in which both roughness and defects appear, the distribution of non-local Dang Van stress is plotted in Fig. 18. With an R* value set to 60 μm, no evident difference can be found between the plastic and elastic model.

A comprehensive comparison is performed for all the defective models. In the three configurations, the relative responses of fatigue prediction in the plastic model compared to the one in the elastic model under a cyclic tension loading at 150 MPa are listed in Table 8. It should be noted that certain data are not available since the convergence is not reached in those configurations. Roughness which can be considered as a series of small defects has the smallest difference after adding plasticity in simulation. Nevertheless, even if the large geometrical defects are combined with the surface roughness, the generated results do not significantly change. Different R* are compared. Generally, as the R* increases, the difference between the plastic model and elastic model decreases. Overall, introducing the plasticity to the constitutive model in current simulation framework does not lead to a significant change if the considered effective area is relatively large.

5.3. Summary

The introduction of plasticity to the current simulation framework does not bring significant differences in the yielded fatigue predictions. All comparisons are performed between models with the same configuration except the constitutive models. In the smooth models, the plastic zone originates at the grain boundaries because of the heterogeneous microstructural texture. The isotropically textured smooth model exhibits local plastic deformations in certain places at its macroscopic fatigue limit. And it is more noticeable in the model with realistic texture. But in terms of fatigue prediction, the difference between models with or without plasticity is insignificant. In the defective models, the defect brings a strong stress concentration at its root which causes plastic deformation. Due to lower macroscopic loading levels compared to the ones for smooth models, the plastic deformation from microstructure heterogeneity is not noticeable. The accumulated plastic deformation at the grain boundaries is thus less in these configurations. Overall, the role of plasticity in the defective model is also negligible.

Without using the plastic constitutive model, the prediction of fatigue failure can still be achieved by using the cubic elastic constitutive model. On one hand, the scatter of local mechanical responses in polycrystalline aggregate is mainly due to the anisotropy of microstructure which in this study is brought by the explicit grain and texture. The adoption of plasticity provides a more accurate description of the stress state in certain highly stressed places. But in the context of high cycle fatigue, the macroscopic loading is in the elastic domain. So, the existence of plastic deformation is limited. On the other hand, with a relatively large R* applied, the stress distribution in the effective area is not notably changed as the plastic deformation only occurs in the local area near the grain boundary.

6. Conclusions

An extended explicit microstructure sensitive finite element modeling approach is proposed and is adopted to an additive manufactured 316L. The established numerical model takes the surface defect and typical microstructural attributes into consideration at the same time. Since the experimental results mostly present the combining competitive effects of defects and microstructure, simulations are conducted to distinguish these controlling parameters.

Results show that LoF defect is the most detrimental factor in HCF failure. LoF defects are dominant over texture, roughness and grain size and morphology. Microstructure texture has a noticeable effect. The preferential grain orientation on the fatigue behavior of SLM SS 316L is found to reduce the endurance limit by 10%. When LoF defects exist on or near the surface, roughness measured in the fabricated specimen has no perceptible influence on fatigue strength. Without the presence of LoF defect, among the characteristic parameters of roughness, Rv shows certain relevance with the predicted fatigue limit.

Several preliminary tests have been performed to check the effect of plasticity in the current simulation framework. Results show that for the studied material, disregarding plasticity reduces the computational expense without losing the fidelity of outputs.

Declaration of Competing Interest

The authors declare that they have no known competing financial interests or personal relationships that could have appeared to influence the work reported in this paper.

References

[1] Tolosa I, Garciandía F, Zubiri F, Zapirain F, Esnaola A. Study of mechanical properties of AISI 316 stainless steel processed by "selective laser melting", following different manufacturing strategies. Int J Adv Manuf Technol 2010;51(5-8):639–47. https://doi.org/10.1007/s00170-010-2631-5.

[2] Cherry JA, Davies HM, Mehmood S, Lavery NP, Brown SGR, Sienz J. Investigation into the effect of process parameters on microstructural and physical properties of 316L stainless steel parts by selective laser melting. Int J Adv Manuf Technol 2015;76(5-8):869–79. https://doi.org/10.1007/s00170-014-6297-2.

[3] Gokuldoss PK, Kolla S, Eckert J. Additive manufacturing processes: Selective laser melting, electron beam melting and binder jetting-selection guidelines. Materials (Basel) 2017;10(6):672. https://doi.org/10.3390/ma10060672.

[4] Afkhami S, Dabiri M, Alavi SH, Björk T, Salminen A. Fatigue characteristics of steels manufactured by selective laser melting. Int J Fatigue 2019;122:72–83. https://doi.org/10.1016/j.ijfatigue.2018.12.029.

[5] DebRoy T, Wei HL, Zuback JS, Mukherjee T, Elmer JW, Milewski JO, et al. Additive manufacturing of metallic components – Process, structure and properties. Prog Mater Sci 2018;92:112–224. https://doi.org/10.1016/j.pmatsci.2017.10.001.

[6] Spierings AB, Starr TL, Wegener K. Fatigue performance of additive manufactured metallic parts. Rapid Prototyp J 2013;19(2):88–94. https://doi.org/10.1108/13552541311302932.

[7] Uhlmann E, Fleck C, Gerlitzky G, Faltin F. Dynamical Fatigue Behavior of Additive Manufactured Products for a Fundamental Life cycle Approach. Proc CIRP 2017;61:588–93. https://doi.org/10.1016/j.procir.2016.11.138.

[8] Shrestha R, Simsiriwong J, Shamsaei N. Fatigue behavior of additive manufactured 316L stainless steel parts: Effects of layer orientation and surface roughness. Addit Manuf 2019;28:23–38. https://doi.org/10.1016/j.addma.2019.04.011.

[9] Yadollahi A, Shamsaei N. Additive manufacturing of fatigue resistant materials: Challenges and opportunities. Int J Fatigue 2017;98:14–31. https://doi.org/10.1016/j.ijfatigue.2017.01.001.

[10] Blinn B, Krebs F, Ley M, Teutsch R, Beck T. Determination of the influence of a stress-relief heat treatment and additively manufactured surface on the fatigue behavior of selectively laser melted AISI 316L by using efficient short-time procedures. Int J Fatigue 2020;131:105301. https://doi.org/10.1016/j.ijfatigue.2019.105301.

[11] Riemer A, Leuders S, Thöne M, Richard HA, Tröster T, Niendorf T. On the fatigue crack growth behavior in 316L stainless steel manufactured by selective laser melting. Eng Fract Mech 2014;120:15–25. https://doi.org/10.1016/j.engfracmech.2014.03.008.

[12] Mower TM, Long MJ. Mechanical behavior of additive manufactured, powder-bed laser-fused materials. Mater Sci Eng A 2016;651:198–213. https://doi.org/10.1016/j.msea.2015.10.068.

[13] Blinn B, Ley M, Buschhorn N, Teutsch R, Beck T. Investigation of the anisotropic fatigue behavior of additively manufactured structures made of AISI 316L with short-time procedures PhyBaL LIT and PhyBaL CHT. Int J Fatigue 2019;124:389–99. https://doi.org/10.1016/j.ijfatigue.2019.03.022.

[14] Liverani E, Toschi S, Ceschini L, Fortunato A. Effect of selective laser melting (SLM) process parameters on microstructure and mechanical properties of 316L austenitic stainless steel. J Mater Process Technol 2017;249:255–63. https://doi.org/10.1016/j.jmatprotec.2017.05.042.

[15] Zhang M, Sun C-N, Zhang X, Goh PC, Wei J, Hardacre D, et al. Fatigue and fracture behaviour of laser powder bed fusion stainless steel 316L: Influence of processing parameters. Mater Sci Eng A 2017;703:251–61. https://doi.org/10.1016/j.msea.2017.07.071.

[16] Przybyla C, Prasannavenkatesan R, Salajegheh N, McDowell DL. Microstructure-sensitive modeling of high cycle fatigue. Int J Fatigue 2010;32(3):512–25. https://doi.org/10.1016/j.ijfatigue.2009.03.021.

[17] McDowell DL, Dunne FPE. Microstructure-sensitive computational modeling of fatigue crack formation. Int J Fatigue 2010;32(9):1521–42. https://doi.org/10.1016/j.ijfatigue.2010.01.003.

[18] Liang X, Robert C, Hor A, Morel F. A numerical investigation of the high cycle fatigue sensitivity to microstructure and defect. Int J Fatigue 2020;136:105541. https://doi.org/10.1016/j.ijfatigue.2020.105541.

[19] Susmel L, Taylor D. A simplified approach to apply the theory of critical distances to notched components under torsional fatigue loading. Int J Fatigue 2006;28(4):417–30. https://doi.org/10.1016/j.ijfatigue.2005.07.035.

[20] Hor A, Saintier N, Robert C, Palin-Luc T, Morel F. Statistical assessment of multiaxial HCF criteria at the grain scale. Int J Fatigue 2014;67:151–8. https://doi.org/10.1016/j.ijfatigue.2014.01.024.

[21] Przybyla CP, McDowell DL. Microstructure-sensitive extreme-value probabilities of high-cycle fatigue for surface vs. subsurface crack formation in duplex Ti-6Al-4V. Acta Mater 2012;60(1):293–305. https://doi.org/10.1016/j.actamat.2011.09.031.

[22] Quey R, Dawson PR, Barbe F. Large-scale 3D random polycrystals for the finite element method: Generation, meshing and remeshing. Comput Methods Appl Mech Eng 2011;200(17-20):1729–45. https://doi.org/10.1016/j.cma.2011.01.002.

[23] Tekçe N, Fidan S, Tuncer S, Kara D, Demirci M. The effect of glazing and aging on the surface properties of CAD/CAM resin blocks. J Adv Prosthodont 2018;10:50–7. https://doi.org/10.4047/jap.2018.10.1.50.

[24] Solberg K, Guan S, Razavi SMJ, Welo T, Chan KC, Berto F. Fatigue of additively manufactured 316L stainless steel: The influence of porosity and surface roughness. Fatigue Fract Eng Mater Struct 2019;42(9):2043–52. https://doi.org/10.1111/ffe.v42.910.1111/ffe.13077.

[25] Elangeswaran C, Cutolo A, Muralidharan GK, de Formanoir C, Berto F, Vanmeensel K, et al. Effect of post-treatments on the fatigue behaviour of 316L stainless steel manufactured by laser powder bed fusion. Int J Fatigue 2019;123:31–9. https://doi.org/10.1016/j.ijfatigue.2019.01.013.

[26] Murakami Y. Metal Fatigue: Effects of Small Defects and Nonmetallic Inclusions. Oxford: Elsevier Science Ltd; 2002.

[27] El Khoukhi D, Morel F, Saintier N, Bellett D, Osmond P, Le V-D, et al. Experimental investigation of the size effect in High Cycle Fatigue: role of the defect population in cast aluminium alloys. Int J Fatigue 2019;129:105222. https://doi.org/10.1016/j.ijfatigue.2019.105222.

[28] Le VD, Saintier N, Morel F, Bellett D, Osmond P. Investigation of the effect of porosity on the high cycle fatigue behaviour of cast Al-Si alloy by X-ray micro-tomography. Int J Fatigue 2018;106:24–37. https://doi.org/10.1016/j.ijfatigue.2017.09.012.

[29] Romano S, Miccoli S, Beretta S. A new FE post-processor for probabilistic fatigue assessment in the presence of defects and its application to AM parts. Int J Fatigue 2019;125:324–41. https://doi.org/10.1016/j.ijfatigue.2019.04.008.

[30] Mergulhão MV, Das Neves MDM. Characteristics of Biometallic Alloy to Additive Manufacturing Using Selective Laser Melting Technology. J Biomater Nanobiotechnol 2018;09(01):89–99. https://doi.org/10.4236/jbnb.2018.91008.

[31] Geuzaine C, Remacle J-F. Gmsh: A 3-D finite element mesh generator with built-in pre- and post-processing facilities. Int J Numer Methods Eng 2009;79(11):1309–31. https://doi.org/10.1002/nme.2579.

[32] Huntington HB. The Elastic Constants of Crystals. Solid State Phys - Adv Res Appl 1958;7:213–351. https://doi.org/10.1016/S0081-1947(08)60553-6.

[33] Méric L, Cailletaud G, Gaspérini M. calculations of copper bicrystal specimens submitted to tension-compression tests. Acta Metall Mater 1994;42(3):921–35. https://doi.org/10.1016/0956-7151(94)90287-9.

[34] Robert C, Mareau C. A comparison between different numerical methods for the modeling of polycrystalline materials with an elastic-viscoplastic behavior. Comput Mater Sci 2015;103:134–44. https://doi.org/10.1016/j.commatsci.2015.03.028.

[35] Deb K, Pratap A, Agarwal S, Meyarivan T. A fast and elitist multiobjective genetic algorithm: NSGA-II. IEEE Trans Evol Comput 2002;6:182–97. https://doi.org/10.1109/4235.996017.

[36] Dang Van K, Cailletaud G, Flavenot JF, Le DA, Lieurade HP. Criterion for High Cycle Fatigue Failure Under Multuiaxial Loading. Biaxial and Multiaxial Fatigue 1989:459–78.

[37] Papadopoulos IV, Panoskaltsis VP. Invariant formulation of a gradient dependent multiaxial high-cycle fatigue criterion. Eng Fract Mech 1996;55(4):513–28. https://doi.org/10.1016/S0013-7944(96)00047-1.

[38] Morel F, Huyen N. Plasticity and damage heterogeneity in fatigue. Theor Appl Fract Mech 2008;49(1):98–127. https://doi.org/10.1016/j.tafmec.2007.10.006.

[39] Guerchais R, Morel F, Saintier N. The effect of the microstructure and defects on crack initiation in 316L stainless steel under multiaxial high cycle fatigue. Adv Mater Res 2014;891-892:815–20. https://doi.org/10.4028/www.scientific.net/AMR.891-89210.4028/www.scientific.net/AMR.891-892.815.

[40] Guerchais R, Morel F, Saintier N, Robert C. Influence of the microstructure and voids on the high-cycle fatigue strength of 316L stainless steel under multiaxial loading. Fatigue Fract Eng Mater Struct 2015;38:1087–104. https://doi.org/10.1111/ffe.12304.

[41] Elangeswaran C, Cutolo A, Muralidharan GK, Vanmeensel K, Van Hooreweder B. Microstructural analysis and fatigue crack initiation modelling of additively manufactured 316L after different heat treatments. Mater Des 2020;194:108962. https://doi.org/10.1016/j.matdes.2020.108962.

[42] Fisher RA, Tippett LHC. Limiting forms of the frequency distribution of the largest or smallest member of a sample. Math Proc Cambridge Philos Soc 1928;24(2):180–90. https://doi.org/10.1017/S0305004100015681.

[43] Freudenthal AM, Gumbel EJ. Minimum Life in Fatigue. J Am Stat Assoc 1954;49(267):575–97. https://doi.org/10.1080/01621459.1954.10483522.

[44] Jenkinson AF. The frequency distribution of the annual maximum (or minimum) values of meteorological elements. Q J R Meteorol Soc 1955;81(348):158–71. https://doi.org/10.1002/(ISSN)1477-870X10.1002/qj.v81:34810.1002/qj.49708134804.

[45] Vayssette B, Saintier N, Brugger C, El MM, Pessard E. Numerical modelling of surface roughness effect on the fatigue behavior of Ti-6Al-4V obtained by additive manufacturing. Int J Fatigue 2019;123:180–95. https://doi.org/10.1016/j.ijfatigue.2019.02.014.

[46] Guilhem Y, Basseville S, Curtit F, Stéphan J-M, Cailletaud G. Investigation of the effect of grain clusters on fatigue crack initiation in polycrystals. Int J Fatigue 2010;32(11):1748–63. https://doi.org/10.1016/j.ijfatigue.2010.04.003.